Microporous and Mesoporous Materials 402 (2026) 113994

Contents lists available at ScienceDirect

Microporous and Mesoporous Materials

journal homepage: www.elsevier.com/locate/micromeso

Optimising the structure of mesoporous niobium oxide using evaporation-induced self-assembly synthesis method

Peter Nadrah [a,*], Mateja Knap [a], Erika Švara Fabjan [a], Andraž Šuligoj [b,c], Urška Lavrenčič Štangar [b], Goran Dražić [c], Nataša Novak Tušar [c,d], Andrijana Sever Škapin [a,e]

[a] Slovenian National Building and Civil Engineering Institute, Dimičeva Ulica 12, 1000, Ljubljana, Slovenia
[b] University of Ljubljana, Faculty of Chemistry and Chemical Technology, Večna Pot 113, 1000, Ljubljana, Slovenia
[c] National Institute of Chemistry, Hajdrihova Ulica 19, 1000, Ljubljana, Slovenia
[d] University of Nova Gorica, Vipavska Cesta 13, 5000, Nova Gorica, Slovenia
[e] Faculty of Polymer Technology, Ozare 19, 2380, Slovenj Gradec, Slovenia

ARTICLE INFO

Keywords:
Nb_2O_5
Mesoporous material
Evaporation-induced self-assembly
Photocatalysis

ABSTRACT

To increase the photocatalytic performance of Niobium(V) oxide (Nb_2O_5) it is necessary to increase its accessible surface area. The evaporation-induced self-assembly (EISA) synthesis method is well suited for the synthesis of mesoporous structures, but the optimisation of synthesis parameters for Nb_2O_5 is still limited. In this study, we demonstrate that the synthesis parameters — duration of evaporation, airflow rate, relative humidity and water content in the reaction mixture — significantly affect the specific surface area, mesoporous structure and photocatalytic performance of isopropanol oxidation into acetone of Nb_2O_5. Our results show that a combination of long evaporation duration, low airflow rate, low relative humidity and moderate water content are needed to obtain material with the highest specific surface area (145 $m^2\ g^{-1}$) and a narrow hysteresis loop in the N_2 sorption isotherm. This material exhibits four times higher photocatalytic activity compared to materials synthesised under less favourable conditions (14.3–17.7 μmol h^{-1} compared to 3.7 μmol h^{-1}). We also show that the ordered mesoporous structure plays an important role in improving the photocatalytic performance: the materials with a higher degree of order exhibit about two times higher activity than the materials with a lower degree of order with the same specific surface area (10.4–12.1 μmol h^{-1} compared to 4.9–7.9 μmol h^{-1}). These results provide valuable insights for optimising the synthesis of mesoporous niobium oxide to increase both the specific surface area and photocatalytic performance.

1. Introduction

Niobium oxides exist in several oxidation states of niobium; the most common stoichiometric is niobium pentoxide (Nb_2O_5) — an *n*-type semiconductor that has garnered significant research interest in catalysis [1] due to its unique physicochemical properties, including a wide bandgap (~3.4 eV), non-toxicity, surface acidity and the natural abundance of niobium [2]. These features make Nb_2O_5 a promising material for applications in sensor technology, catalysis and photoelectrochemistry [2]. Nb_2O_5 crystallises in several polymorphs, with the most common being monoclinic (H-Nb_2O_5), orthorhombic (T-Nb_2O_5) and pseudo-hexagonal (TT-Nb_2O_5) [3]. Amorphous Nb_2O_5, on the other hand, does not have well-established structure and possesses NbO_6, NbO_7 and NbO_8 units [4,5]. Strong acidity of the surface is a unique property of Nb_2O_5, especially of the amorphous phase, and makes it an effective catalyst in acid-catalysed reactions [2]. Recently, Nb_2O_5-based photocatalysts were explored for photoreduction of CO_2 [6], microplastic degradation [7], and H_2 production [8].

The low surface area of bulk Nb_2O_5 limits its practical applications, necessitating the development of nanostructured and porous architectures to enhance its functional performance. A large surface area is crucial for increasing the number of active sites on the surface of the material per unit mass [9]. Mesoporous materials with pore sizes ranging from 2 nm to 50 nm offer advantages over smaller non-porous nanoparticles, including well-defined pore sizes and easier handling due to their larger particle size. Various synthesis methods, including

* Corresponding author.
E-mail address: peter.nadrah@zag.si (P. Nadrah).

https://doi.org/10.1016/j.micromeso.2025.113994
Received 10 November 2025; Received in revised form 8 December 2025; Accepted 11 December 2025
Available online 19 December 2025

soft- and hard-templating approaches [10,11], sol-gel processing [12], combustion [13] and hydrothermal treatments [14], have been employed to fabricate mesoporous Nb_2O_5 and composites with other oxides [15–17] with tunable pore structures and surface functionalities. Recently, Brum et al. [18] reported on green synthesis of Nb_2O_5 using pecan nutshell. The authors noted a lack of established mechanism and complex reaction mixture involving natural extracts. Larison et al. [19] reported on development of block polymers for direct synthesis of heterostructures, TiO_2–Nb_2O_5 and ZrO_2–Nb_2O_5, among others, with interconnected porosity. However, preparing well-ordered mesoporous Nb_2O_5 is not straight-forward. Most reports on the photocatalytic mesoporous Nb_2O_5 exhibit type IV isotherms with the hysteresis loop spanning large p/p^0 range and a low degree of pore order.

The evaporation-induced self-assembly (EISA) method is a convenient approach for synthesising mesoporous materials, particularly metal oxides, with well-ordered porous structure [20–22]. While the relative humidity (RH) of the air above the reaction mixture is a crucial parameter in EISA, it is often unreported or uncontrolled in the syntheses of Nb_2O_5 available in the literature.

In the late 1990s, Ying and co-workers reported on the synthesis of the well-ordered Nb_2O_5 using surfactants with C12 to C18 hydrophobic chain [23]. They obtained Nb_2O_5 with either hexagonal, cubic or layer porous structure. Shortly afterwards, Stucky and co-workers reported on the mesoporous Nb_2O_5 synthesised using poly(ethylene oxide)-poly (propylene oxide)-poly(ethylene oxide) (PEO-PPO-PEO) copolymers [24]. Although the porous structure was identified as hexagonal based on the micrographs from transmission electron microscope (TEM), the reflections in low-angle diffractograms were not well resolved [25]. In early 2000s, Domen and co-workers synthesised 3D hexagonal mesoporous Nb_2O_5 and demonstrated crucial role of small amount of cations [26]. Later, Liu, Zhao and co-workers reported on Nb_2O_5 thin film with hexagonal mesoporous structure [27,28]. Hexagonal order of the pore openings was observed with TEM, however, calcined materials exhibited much diminished peak intensities in the low-angle region of diffractograms. Yuan and Guliants [29] reported on aging the $NbCl_5$ solution in presence of PEO-PPO-PEO copolymer at 20 % and 70 % RH. At 70 % RH they obtained Nb_2O_5 with larger pores and N_2 sorption analysis suggested more uniform cylindrical mesopores. They postulated higher RH retains water in the reaction mixture, slows the evaporation and thus provides necessary fluidity for organisation of the template molecules. On the other hand, Ye et al. [30] obtained 3D cubic mesoporous Nb_2O_5 at approx. 40 % RH. They stated that RH above 50 % or below 30 % leads to formation of wormhole-like or hexagonal mesoporous Nb_2O_5. While these reports investigated influence of RH; other parameters, such as airflow rate and synthesis duration, are reported less often. These reports also focused on the structure of Nb_2O_5 and not its catalytic activity. Therefore, a relationship between these parameters and catalytic activity needs to be established for optimising the Nb_2O_5 structures for catalytic applications.

To bridge the gap between the reported effects of synthesis conditions on the structure of Nb_2O_5 and the photocatalytic performance of Nb_2O_5, we designed the experiment to study the effects of the synthesis parameters (duration of evaporation, RH, airflow rate and water content) on the structure and photocatalytic performance of mesoporous Nb_2O_5 using the EISA method with soft-templating using PEO-PPO-PEO copolymers.

2. Experimental

2.1. Materials

The following chemicals were used in the experiments: niobium(V) chloride (Merck), ethanol (Merck), PEO-PPO-PEO copolymer Pluronic P-123 (Aldrich), purified water (18.2 MΩ cm^{-1}), magnesium(II) chloride (Riedel-de Haën), sodium chloride (Honeywell Fluka), sodium hydroxide (Honeywell Fluka), 1-butanol (Sigma-Aldrich), barium sulfate (Fluka), potassium bromide (Honeywell Fluka), fuming (37 %) hydrochloric acid (Merck Supelco).

2.2. Synthesis

Nb_2O_5 materials were prepared via EISA approach under controlled conditions followed by calcination. The following synthesis parameters were varied: 1) amount of water in the reaction mixture, 2) duration of the synthesis, 3) relative humidity in the reaction chamber and 4) airflow rate. First, Pluronic P123 (0.85 g, 0.15 mmol, 0.02 equiv.) was added to ethanol (12.9 mL, 221 mmol, 30 equiv.) and stirred in a 100 mL round bottom flask at 40 °C for 30 min. $NbCl_5$ (1.98 g, 7.4 mmol, 1 equiv.) was then added to the solution, which turned yellow and then back to transparent in a few seconds. After 10 min, a mixture of ethanol (4.3 mL, 74 mmol, 10 equiv.) and water (0 mmol, 74 mmol or 147 mmol corresponding to 0 equiv., 10 equiv. or 20 equiv.) was slowly added to the reaction mixture and stirred for 30 min. The reaction mixture was transferred to two crucibles and placed in the chamber. The chamber was placed in a dryer at a temperature of 40 °C for 23 or 69 h to evaporate the solvents and acid by-product. RH in the chamber was obtained by airflow through a saturated aqueous solution of a salt: $MgCl_2$ for ~33 % RH and NaCl for ~65 % RH. The airflow rate was controlled by the voltage supplied to the air pump: 31 mL s^{-1} or 79 mL s^{-1}. Afterwards, the obtained white gel was thermally treated at 400 °C for 4 h with a ramp of 1 °C·min^{-1} in air. Finally, the material was crushed for 10 min in an agate mortar.

2.3. Characterisation

For nitrogen sorption analysis, approximately 80 mg of the sample was accurately weighted into the analysis tube, dried at 105 °C under vacuum and then analysed at approx. −196 °C (77 K) using Micromeritics ASAP 2020. Brunauer–Emmett–Teller (BET) surface area was determined between 0.05 and 0.35 p/p_0. Pore sizes were calculated using Barrett–Joyner–Halenda (BJH) model with Kruk–Jaroniec–Sayari (KJS) correction and KJS thickness curve from the adsorption branch.

Concentration of acidic sites on the surface of materials were determined by neutralisation with excess base and then back-titrated with an acid via a modified method from the literature [10,31]. Accurately weighted approx. 50 mg of the sample was dispersed in 10 mL 0.04 M aqueous solution of NaOH, placed in an ultrasonic bath for 30 s and stirred overnight. The suspension was centrifuged, and 8 mL of the supernatant was transferred into a beaker and approx. 20 mL of water was added. The solution was titrated with 0.04 M hydrochloric acid until pH 7.

Low-angle and high-angle X-ray powder diffraction (XRD) measurements were performed on a PANalytical Empyrean using a $CuK_{\alpha1}$ with wavelength of 1.5406 Å. The patterns were measured with a step of 0.013° 2Θ and integration time of 100 s.

TEM analysis was conducted using a Jeol ARM 200 CF probe Cs-corrected Scanning TEM, which is equipped with Jeol Centurio energy-dispersive X-ray spectroscopy (EDXS) and Gatan dual electron energy loss spectroscopy (EELS) systems.

Energy dispersive X-ray spectroscopy (EDS) analysis was performed on Thermo Fisher Scientific Apreo 2.

Spectra of X-ray photoelectron spectroscopy (XPS) were collected using a PHI VersaProbe III (version AD) equipped with a hemispherical analyser and a monochromatic Al Kα X-ray source. Survey spectra were measured using a pass energy of 160 eV with a step of 1 eV s^{-1}.

Fourier-transform infrared spectroscopy (FTIR) was performed on the samples prepared as 0.2 wt% mixture with KBr and pressed into pallets. The analysis was done on PerkinElmer Spectrum Two with pure KBr for the background.

For Raman spectroscopy, the samples were pressed into the sample holder and the spectra were acquired using a Bruker BRAVO Raman spectrometer. Tip for direct measurements at small amounts of powder

samples was used and DuoLaser™ excitation (785 nm and 852 nm) was applied to the samples. The spectra were obtained using OPUS software.

Diffuse reflectance spectroscopy (DRS) was performed using PerkinElmer Lambda 1050 with an integrating sphere. The samples were mixed with $BaSO_4$ to 1 wt% and placed in a solid sample holder. The port for the specular component on the integrating sphere was opened to exclude the specular component from the collected spectra. The spectra were collected in reflectance mode and then converted into Tauc plots using Kubelka–Munk transformation. The indirect band gap values were determined by linear fit to the slope in the Tauc plot and then calculated from the intersection of the linear fit with the baseline.

The photocatalytic experiments were conducted in the reactor tracking the oxidation of gaseous isopropanol into acetone. The reactor connected to the gaseous cell on PerkinElmer Spectrum Two FTIR has already been described in detail before [32]. Briefly, approx. 40 mg of the sample was placed in an air-tight reactor with a relative humidity of 33 %. 8 μL of isopropanol was injected and allowed to evaporate. After 1 h, the sample was irradiated with a Xenon lamp (approx. 20 W m^{-2} in 300–400 nm and approx. 240 W m^{-2} in 400–800 nm) using an IR filter. The concentrations of isopropanol and its first oxidation product acetone were measured using FTIR. The photocatalytic activity was calculated as a formation rate of acetone in the first 6 min of irradiation. Conversion rate was calculated as a ratio between the formation rate of acetone and the consumption rate of isopropanol in the same timeframe. Stability testing was conducted over 5 cycles of photocatalytic measurements. The material was exposed to UV light for 30 min per cycle.

3. Results and discussion

We synthesised a series of mesoporous niobium oxides using the EISA method to identify the optimal conditions for obtaining a well-ordered mesoporous structure. We investigated the influence of four synthesis parameters: evaporation duration, airflow rate, relative humidity (RH) and the amount of water in the reaction mixture. In the first part of the study, we synthesised 8 materials with fixed water content (0 equiv.) and varied the other parameters, namely duration, airflow rate and RH. In the second part of the study, we investigated the influence of the amount of water in the reaction mixture with the two selected combination of the other synthesis parameters.

3.1. Effect of evaporation duration, airflow rate and relative humidity

The first 8 materials synthesised to investigate the influence of evaporation duration, airflow rate and RH at a fixed water amount (0 equiv.) are summarized in Table 1. The two chosen values of each quantity reflect the low and high values determined from preliminary experiments and the literature [9,33]. Testing of all combinations of the values allowed us study the effect of each quantity independently. For brevity, we will refer to duration in days (1 and 3 days as approximation of 23 h and 69 h, respectively) and to airflow rate as low and high (low and high for 31 mL s^{-1} and 79 mL s^{-1}, respectively). The values of duration and airflow rate were chosen to exhibit similar factor of increase in each parameter (3 and 2.5 for duration and airflow rate, respectively). This allowed us to have roughly comparable amount of air passed through the reactor in the case of 23 h at 79 mL s^{-1} (1 day, high airflow rate) as in the case of 69 h at 31 mL s^{-1} (3 days, low airflow rate), both referred to as medium amount of air volume. After the synthesis in the reactor, the materials were calcined in an oven at 400 °C in air.

Table 1
List of the first 8 materials synthesised to investigate the influence of evaporation duration, airflow rate and RH at a fixed water amount (0 equiv.). RH value of 65 % is approximate. Air volume refers to the volume of air passed through the reactor during the reaction.

Material name	Evaporation duration	Airflow rate	RH	Air volume
	[h]	[mL·s^{-1}]	[%]	[10^3 L]
N-1	23	31	33	2.6 (low)
N-2	23	79	33	6.5 (medium)
N-3	69	31	33	7.7 (medium)
N-4	69	79	33	19.6 (high)
N-5	23	31	65	2.6 (low)
N-6	23	79	65	6.5 (medium)
N-7	69	31	65	7.7 (medium)
N-8	69	79	65	19.6 (high)

We analysed the mesoporous structure using N_2 sorption. All materials synthesised at 33 % RH exhibit type IVa isotherms according to IUPAC (Fig. 1A). Adsorption of N_2 at low relative pressures suggests the presence of micropores. Three materials show isotherms with similar shape: long hysteresis loop spanning from 0.4 p/p_0 to almost saturation, which is best described as H2 type. N-3 stands out with narrower hysteresis loop with steeper slopes in 0.4–0.6 p/p_0 region with the hysteresis of the type H1 with some features of H2. N-1, N-2 and N-4 exhibit also similar pore size distribution with a peak at around 5 nm (Fig. 1B). On the other hand, N-3 has a peak at 6.2 nm. Of the materials synthesised at approx. 65 % RH, N-6 and N-7 (both medium air volume) feature similar isotherms to those of N-1, N-2 and N-4 (Fig. 2A). N-5 exhibits similar shape, but the curve is shifted towards higher amounts of adsorbed N_2. N-8 shows completely different curve with the largest part of the hysteresis loop above 0.7 p/p_0 with hysteresis of the type H4. Although the shape is similar to type H3 hysteresis, the slight decline of the desorption branch distinguished it from the H3 type usually provided as a reference. [34–36] This type of isotherm can still be classified as type IV, since the characteristic saturation plateau can be reduced to an inflection point [36]. While pore size distribution of N-5 has a peak at 6.6 nm, it is lower and broader than any of the peaks of N-1 through N-4 (Fig. 2B). The peaks of N-6 through N-8 are even lower and broader. N-3 has also the highest specific surface area (S_{BET}) and pore volume (V_{pore}) as summarized in Table 2. Majority of the other materials demonstrate comparable values, while N-7 and N-8 (3 days at high RH) exhibit the lowest S_{BET} of all materials. The results point to lower degree of order for the materials synthesised at high RH.

Regarding the surface concentration of the acid sites, most of the materials exhibit 1.5–2 mmol g^{-1} acid sites (both weak and strong, as the method does not differentiate between them) as listed in Table 2. The values are comparable to the literature values for Nb_2O_5 thermally treated at 400 °C or 500 °C [10,37,38]. N-3 exhibits the highest value at 2.2 mmol g^{-1}, while N-6 and N-8 the lowest at 1.4 mmol g^{-1}. The concentration is dependent on S_{BET} as can be seen in Fig. S1 (Supplementary information): acid site concentration increases linearly with S_{BET}. These values are equivalent to approx. 10 acid sites per 1 nm [2]. Although the method used cannot separately quantify Brønsted and Lewis acid sites, a previous study reported their concentration for mesoporous Nb_2O_5 as 338 and 222 μmol g^{-1}, respectively [39].

We investigated the order of the mesoporous structure using low-angle XRD. Materials N-1 through N-6 exhibit a peak at 1.2° 2θ with varying intensity, as presented in Fig. 3. Three materials exhibit also the second peak: N-1 and N-2 at approx. 1.6° 2θ and N-3 at approx. 2.2° 2θ (see the inset in Fig. 3). Although two peaks are not enough to confirm the order of the pore channels, a narrow first peak and the presence of the second peak suggests higher degree of order in N-3 compared to others. N-7 and N-8 do not exhibit any peaks in low-angle XRD pointing to a low degree of order on the nanometre scale.

XRD analysis showed no peaks in the high-angle diffractograms, pointing to a largely amorphous structure (Fig. S2). This is consistent with the literature, as thermal treatment at 400 °C is too low for crystallization of Nb_2O_5 to occur. Reports showed approx. 500 °C is needed to obtain pseudohexagonal Nb_2O_5 (JCPDS No. 07–0061) [38]. The benefit of amorphous phase is its particularly strong acidic surface, which is more pronounced than in the case of crystalline Nb_2O_5 [2].

In TEM analysis of N-3, hexagonally oriented pore openings can be observed in Fig. 4A and parallel pore channels in Fig. 4B. Conversely, N-7 features unordered pores (Fig. S4). This is consistent with N_2 sorption

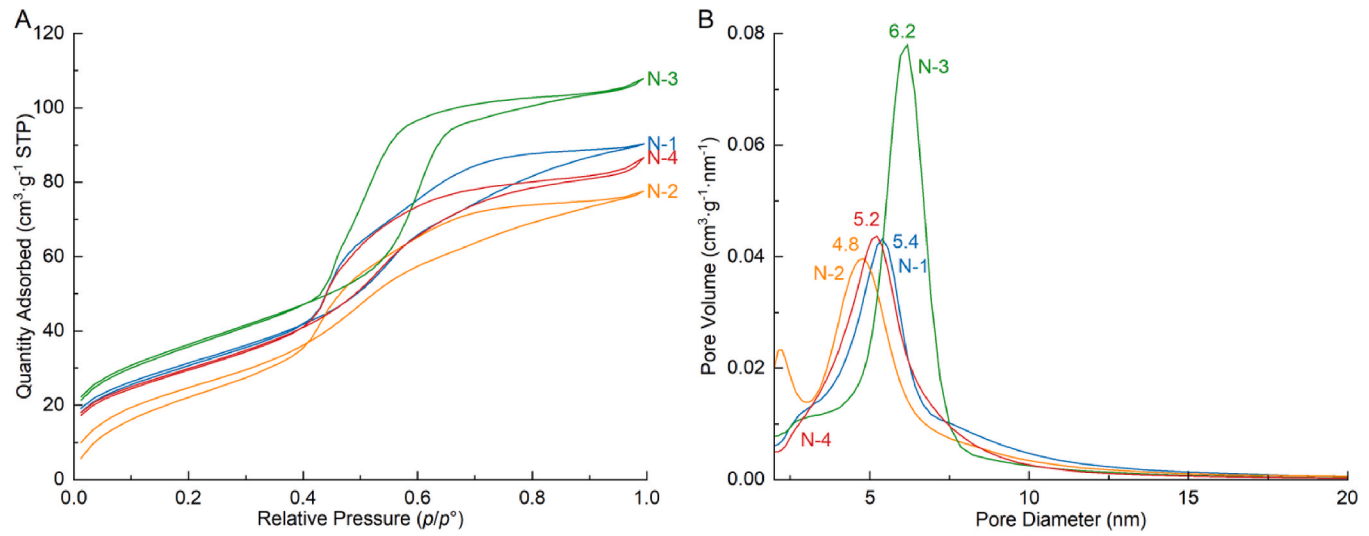

Fig. 1. (A) Nitrogen sorption isotherms and (B) pore size distributions from the adsorption curves of the materials synthesised at 33 % RH. The pore size distribution peaks are marked with a diameter value in nm at the maximum height.

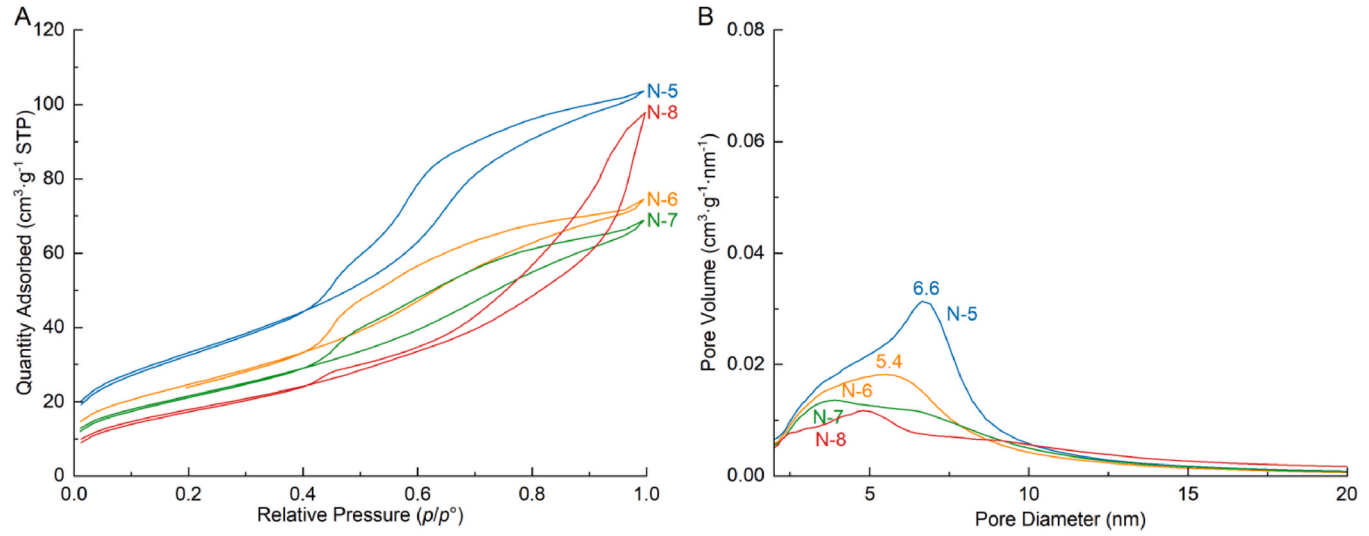

Fig. 2. (A) Nitrogen sorption isotherms and (B) pore size distributions from the adsorption curves of the materials synthesised at approx. 65 % RH. The pore size distribution peaks are marked with a diameter value in nm at the maximum height.

Table 2
S_{BET}, pore volume and acid site concentration of the materials.

Material name	S_{BET} [$m^2 \cdot g^{-1}$]	V_{pore} [$cm^3 \cdot g^{-1}$]	Acid site concentration [$mmol \cdot g^{-1}$]
N-1	112	0.14	1.8
N-2	96	0.12	1.8
N-3	128	0.17	2.2
N-4	109	0.13	1.6
N-5	119	0.16	1.9
N-6	89	0.11	1.4
N-7	78	0.11	1.5
N-8	65	0.14	1.4

and low-angle XRD results pointing to a higher degree of pore order in N-3 and a lower degree in N-7.

XPS analysis of the selected materials (N-2, N-3, N-6 and N-7) revealed only +5 oxidation state of niobium observed in Nb 3d spectra, which feature a doublet of the peaks Nb $3d_{5/2}$ and Nb $3d_{3/2}$ (Fig. S5–S8B). Nb:O ratio is approx. 33:67 in all analysed materials and shows slightly lower content of oxygen compared to the theoretical value of 2:5 (29:71 in percentages) (Table S1). Lower content of oxygen than the theoretical value can be ascribed to oxygen vacancies [40]. The peak in O 1s spectra can be ascribed to contributions from both lattice oxygen and surface oxygen species, located at approx. 530.0 eV and 531.5 eV, respectively (Fig. S5–S8A). The ratio of surface to lattice oxygen is approx. 23:77 and varies only slightly between the materials. Lattice oxygen peak suggests the presence of Nb–O–Nb bonds, while the smaller surface oxygen peak is attributed to surface hydroxyl species and associated with defect sites or vacancies, which have been shown to have a positive effect on the photocatalytic activity [41].

FTIR spectra in Fig. S11 show characteristic band for Nb_2O_5 between 500 cm^{-1} and 1100 cm^{-1} [42]. The band at 2330 cm^{-1} is due to the atmospheric CO_2 and the band at 1604 cm^{-1} is due to the bending vibrations of hydroxyl groups [43]. The band at 3430 cm^{-1} can be ascribed to the adsorbed water and surface hydroxyl groups. Shoulder at 900 cm^{-1} can be attributed to amorphous Nb_2O_5 [44]. No noticeable bands was observed at 2900 cm^{-1} and 1420 cm^{-1} that could correspond to residual organic species [44].

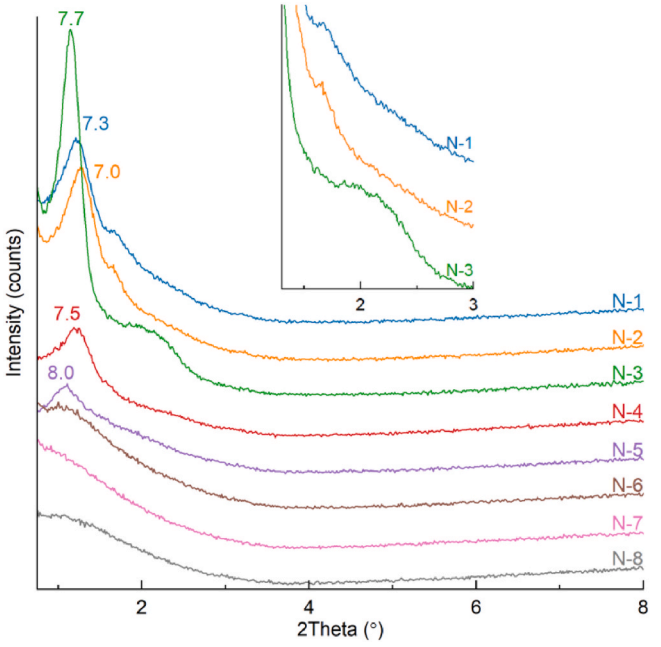

Fig. 3. Diffractograms of N-1 through N-8. Peaks are marked with values of *d*-spacing in nm. Inset shows a close-up of N-1 to N-3. Curves are offset on the y-axis.

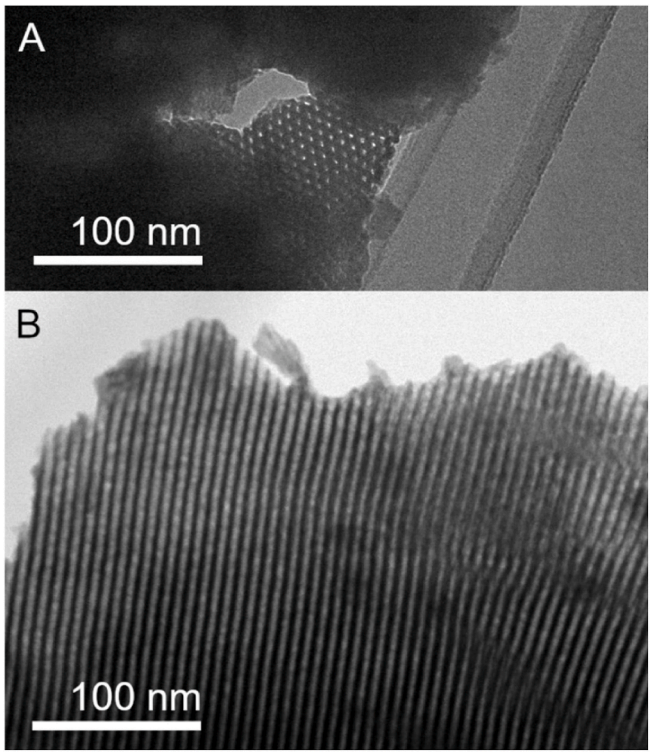

Fig. 4. TEM micrographs of N-3. Hexagonally oriented pore opening can be observed in (A) and parallel pore channels in (B).

Raman spectra in Fig. 5 show two broad peaks, one at around 590 and another at 710 cm^{-1}. The band at 710 cm^{-1} indicates Nb–O stretching vibrations [45,46] in different niobium oxide polyhedra of amorphous Nb_2O_5 [38], particularly with orthorhombic symmetry [47]. The peak at lower wavenumbers is indicative of stretching frequencies for NbO_6 octahedra since its position coincides to its theoretical

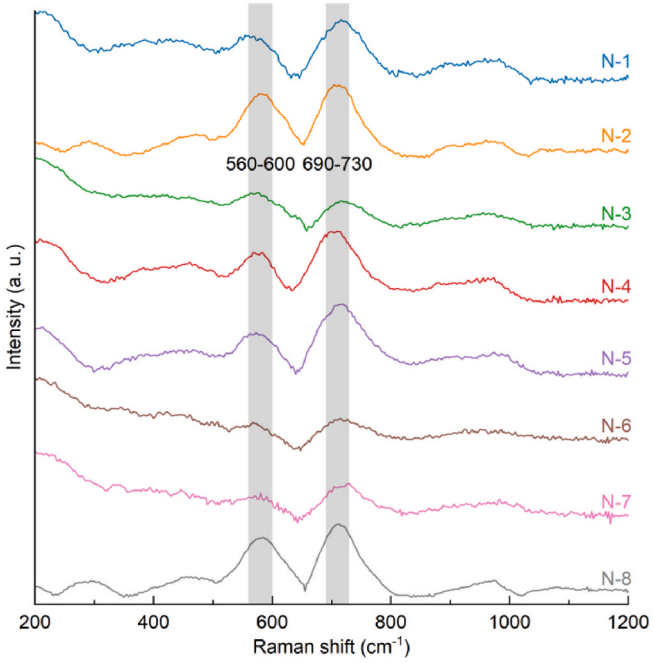

Fig. 5. Normalized Raman spectra. Curves are offset on the y-axis.

calculated value of 586 cm^{-1} [48]. Both peaks belong to Nb–O stretching of slightly distorted NbO_6 octahedra, which are present in amorphous Nb_2O_5 [49].

We recorded the reflectance spectra to calculate the band gap energies of the selected materials (N-2, N-3, N-6 and N-7). Tauc plots presented in Fig. S13 for indirect band gap show of around 3.3 eV (see Table S2), which is close to the reported value of 3.4 eV for Nb_2O_5.

The decrease in the mesoporous order with an increase in RH shows a similar trend to the report by Ye et al. of hexagonal order of pores and worm-like pores below 30 % and above 50 % RH, respectively [30]. This is in contrast to the report of a more uniform mesoporous structure at higher RH (70 % compared to 20 %) [29]. One-day syntheses yielded materials with 88 % of S_{BET} values of the materials from three-day syntheses for both values of airflow rate (at 33 % RH), providing conveniently fast synthesis albeit at the expense of S_{BET} and degree of mesoporous order. For the materials synthesised at 33 % RH, the airflow rate has the most pronounced effect on the mesoporous structure in the three-day syntheses (N-3 and N-4). A lower airflow rate, which supplies water (as water vapour) and causes evaporation of volatile compounds from the reaction mixture at a lower rate, yields materials with an approx. 17 % higher S_{BET} for both one-day and three-day evaporation duration.

3.2. *Effect of water content during synthesis*

In the next part of the study, we investigated the influence of the water amount in the reaction mixture with the two selected combinations of the synthesis parameters, namely combinations used for the materials N-2 and N-3. We selected N-3 parameters since the material displayed the most ordered mesoporous structure according to N_2 sorption and low-angle XRD. Additionally, we selected N-2 parameters for comparison since it was synthesised at the same RH and roughly the same volume of passed air (6.5×10^3 L and 7.7×10^3 L for N-2 and N-3, respectively). The water content in the reaction mixture was increased from 0 to 10 and 20 equiv. (molar equivalents $NbCl_5$:H_2O = 1:X). The list of materials investigated in this context with synthesis parameters are presented in Table 3.

Nitrogen sorption analysis of the N-2 group of materials revealed similar IVa type sorption isotherms, with N-2-20W exhibiting slightly

Table 3
List of the additional four materials synthesised to investigate the influence of water amount and the selected values of duration, airflow rate and RH. N-2 and N-3 have been taken from Table 1 for the sake of comparison.

Material name	Evaporation duration	Airflow rate	RH	Water amount
	[h]	[mL·s^{-1}]	[%]	[equiv.]
N-2	23	79	33	0
N-2-10W	23	79	33	10
N-2-20W	23	79	33	20
N-3	69	31	33	0
N-3-10W	69	31	33	10
N-3-20W	69	31	33	20

longer plateau at high p/p_0 than N-2 (Fig. 6A). Pore size distributions in Fig. 6B show peaks for all materials of N-2 group at about 5 nm. Isotherms of N-3-10W and N-3-20W show similar characteristic as the N-3 isotherm but with much longer plateau above the hysteresis loop (Fig. 7A). The peak height in the pore size distribution in Fig. 7B shifts to slightly higher values (6.2–6.4 nm). S_{BET} and V_{pore} increases with an increasing water content during synthesis reaching 145 m^2 g^{-1} and 0.20 cm^3 g^{-1}, respectively, for N-3-20W (Table 4).

Acid site concentrations of the additional materials stay close to values of the base materials. It decreases slightly for N-2 and increases in the case of N-3 (Table 4).

High-angle XRD showed no peaks in any of the additional materials, pointing again to the largely amorphous structure (Fig. S3). Diffractogram at low angles for N-2 group show a peak at 1.5° 2θ, which becomes less pronounced with increasing water content (Fig. 8). In the case of N-3, diffractograms do not exhibit much difference: the first peak at 1.6° 2θ is similar for all materials of N-3 group, while the second peak is present only as a very broad peak or a shoulder at ~2° 2θ. The presence of only two peaks is insufficient to confirm any order of the mesoporous structure, although hexagonal orientation is suggested for N-3 from the TEM analysis.

TEM of N-3-20W in Fig. 9 show less ordered pores compared to N-3. Unordered array of pore openings can be seen in the upper left side and parallel pores in the bottom right side. Based on the results of N_2 sorption and low-angle XRD, a higher degree of order could be expected in the case of N-3-20W compared to N-3, however, this cannot be evidenced from the TEM micrographs. While some order in mesoporous structure is expected for N-3-20W, since it features a peak in low-angle XRD, TEM analysis does not suggest hexagonal or cubic order of the pores, which have been reported previously for Nb_2O_5 [27,30].

XPS for N-3-10W and N-3-20W show the same peaks as in the case of the first 8 materials (Figs. S9 and S10). Nb:O ratio is also approx. 33:67 in N-3 group of materials (Table S1). EDS analysis showed a ratio 23:77 for N-3-20W (Fig. S14). These results point to slightly oxygen-deficient surface layer compared to bulk composition. However, it can also be a result of underestimation of oxygen by EDS. Surface to lattice oxygen ratio show little variation in N-3 group (Table S1).

Peaks in Raman spectra of N-3-10W and N-3-20W are resolved better than in the case of N-3 (Fig. 10). The peak at 710 cm^{-1} is increasing in intensity with increasing amount of water in the reaction mixture compared to the peak at 570 cm^{-1}. The latter is shifted to lower values in the case of N-3-20W. It is indicative of Nb–O bond in NbO_6 octahedra, hence the shift from octahedral to more polyhedral structure is noted.

The reflectance spectra for N-3-10W and N-3-20W (Fig. S13C and D) show values of around 3.3 eV for indirect band gap (Table S2), which is in line with the results for the N-3.

The results of the effect of the water content show an increase in S_{BET} in the case of a three-day synthesis with a low airflow rate (N-3 group) and to a certain extent also in the case of a one-day synthesis with a high airflow rate (N-2 group). Although the presence of water increases S_{BET}, it distorts the arrangement of the pores (N-3-20W compared to N-3). These results indicate that the presence of water can be beneficial and cannot be replaced by water vapour supplied by the air (at least not by the air with the RH as high as 65 %).

3.3. Photocatalytic performance

To demonstrate a potential use, we evaluated the photocatalytic performance of the materials for the reaction of oxidation of isopropanol into acetone. The mechanism of photooxidation of isopropanol on Nb_2O_5 was proposed by Shishido [50]: an electron is transferred from the adsorbed alcoholate to the conduction band, thus reducing Nb^{5+} to Nb^{4+}. The alkenyl radical is dehydrogenated to carbonyl, which is desorbed from the surface. Nb^{4+} is then reoxidised with molecular oxygen. The rate-determining step is desorption of the carbonyl compounds. The photocatalytic activity was calculated from the formation rate of acetone under irradiation with UV and visible light. The activity of the materials N-1 through N-4 is higher than that of N-5 through N-8 (Fig. 11). Among these materials, N-2 and N-3 exhibit the highest activity. Of the additional materials, N-3-10W and N-3-20W have even higher activity compared to N-3. The activity follows the S_{BET} well, as shown in Fig. 11. The activity increases linearly with S_{BET} for the three groups of the materials (N-5 through N-8, N-2 group, and N-3 group).

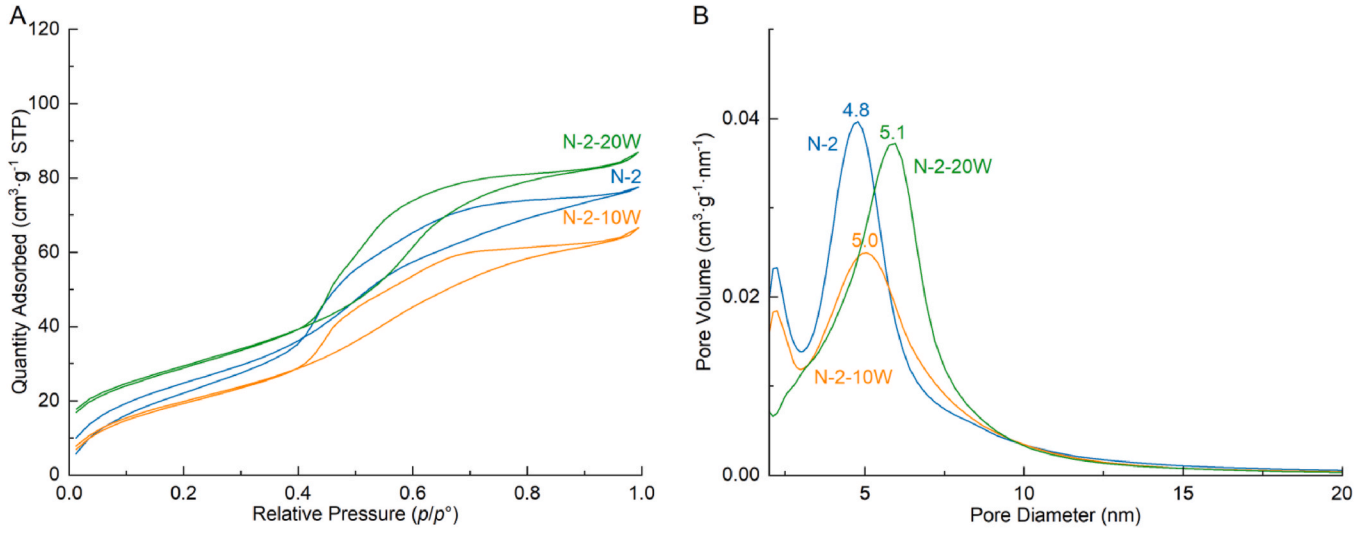

Fig. 6. Nitrogen sorption isotherms (A) and pore size distributions from the adsorption curve (B) of the N-2 group of materials. Pore size distribution peaks are marked with a diameter value in nm at the maximum height.

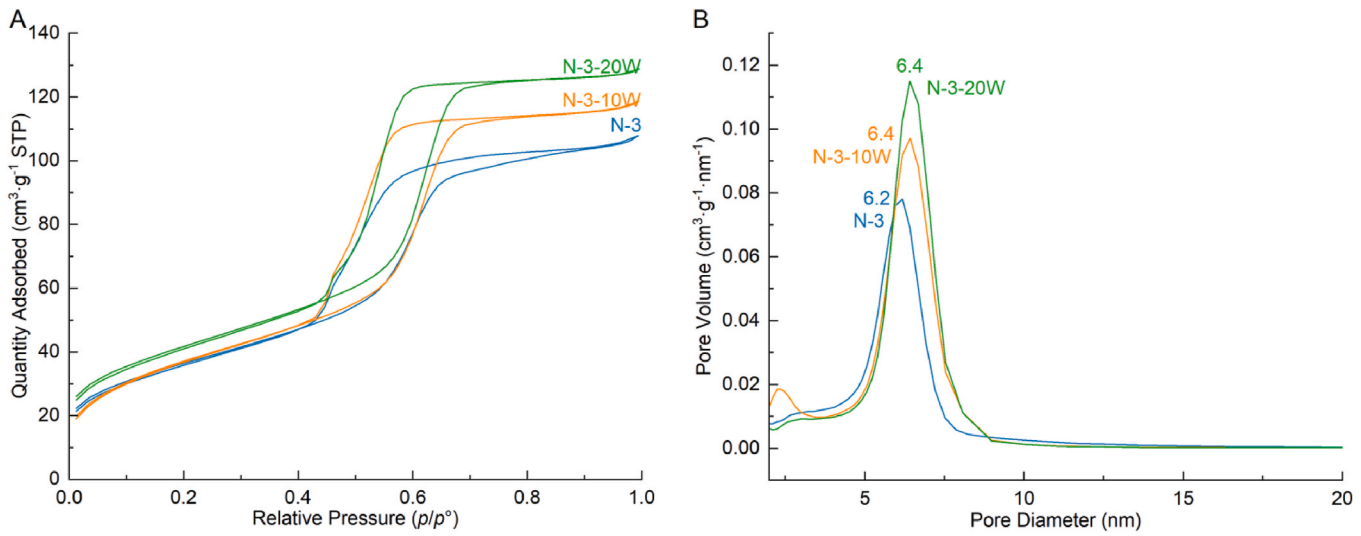

Fig. 7. Nitrogen sorption isotherms (A) and pore size distributions from the adsorption curve (B) for N-3 group of materials. Peaks are marked with a pore diameter value in nm at the maximum height.

Table 4
S_{BET}, pore volume and acid site concentration of the materials. Values for N-2 and N-3 have been taken from Table 2 for the sake of comparison.

Material name	S_{BET} [$m^2 \cdot g^{-1}$]	V_{pore} [$cm^3 \cdot g^{-1}$]	Acid site concentration [$mmol \cdot g^{-1}$]
N-2	96	0.12	1.8
N-2-10W	78	0.10	1.5
N-2-20W	105	0.13	1.7
N-3	128	0.17	2.2
N-3-10W	132	0.18	2.3
N-3-20W	145	0.20	2.4

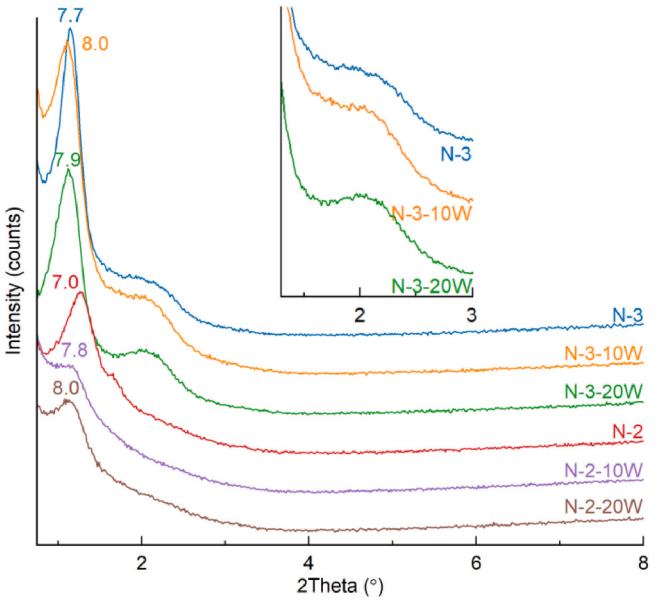

Fig. 8. Diffractograms of the materials of N-2 and N-3 groups. Peaks are marked with values of *d*-spacing in nm. Inset shows a close-up for N-3 group. Curves are offset on the y-axis.

The main reason for the higher activity of the N-3 group can be attributed to higher S_{BET} values compared to the other materials. S_{BET} alone, however, cannot explain the difference between N-5 through N-8 and

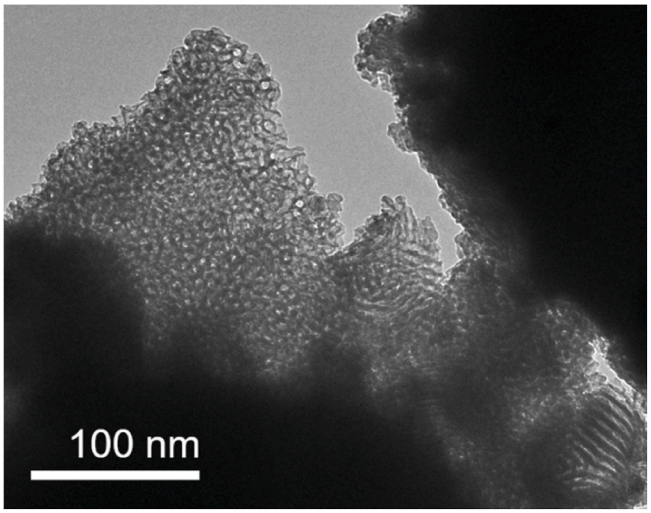

Fig. 9. TEM micrographs of N-3-20W. Unordered array of pore openings can be seen in the upper left side and some parallel pores in the bottom right side.

N-2 group, which have comparable S_{BET}, but the latter has two-fold higher activity. One of the differences between these materials is evident from the N_2 sorption and low-angle XRD: N-2 group has narrower pore size distribution and higher order of mesoporous structure. Furthermore, synthesis at high RH could be responsible for the differences in the surface properties for materials N-5 through N-8. It was reported that increased Brønsted acidity correlated with catalytic propene formation in NbO_x/ZrO_2 [51]. N-3 group had slightly higher acid site concentration than other materials (Fig. S15), however plotting activity vs. surface acid site concentration (concentration/S_{BET}) does not provide any clear correlation (Fig. S16). Conversion rates of oxidation of isopropanol into acetone were above 70 % for all materials (Fig. S17). One material exhibits a rate of over 100 %, which can be attributed to the limitation of the method, which excludes isopropanol adsorbed onto the photocatalyst from the calculation. Thus, with significant adsorption, the method can overestimate the conversion rate.

To analyse the stability of the photocatalysts under the reaction conditions, we performed cycling of the photocatalytic reaction with the best performing material with each cycle including 30 min of UV irradiation. N-3-20W retained over 90 % of its initial activity over 5 cycles

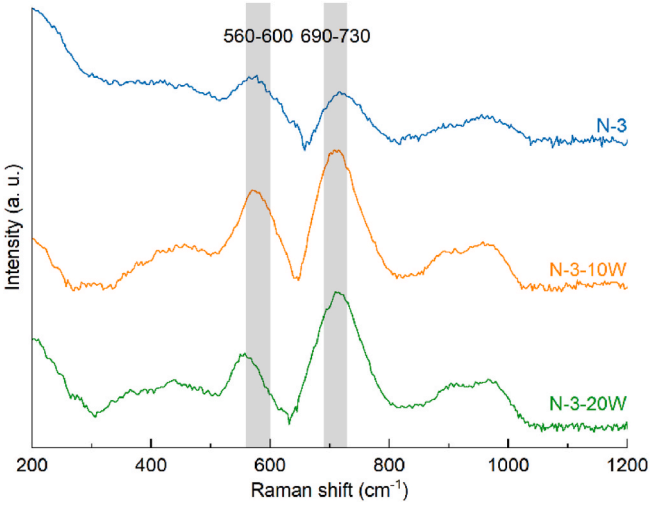

Fig. 10. Normalized Raman spectra of N-3 group of materials. Curves are offset on the y-axis.

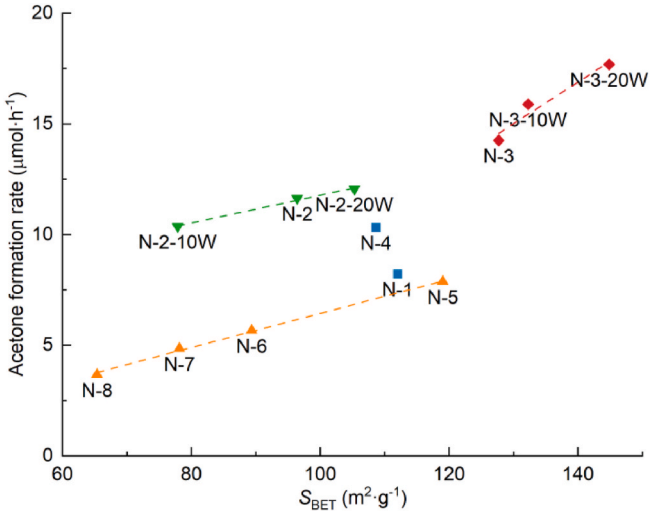

Fig. 11. Photocatalytic activity measured as oxidation of isopropanol into acetone versus S_{BET}. Linear fits connect values for similar materials (N-5 through N-8, N-2 group and N-3 group).

(Fig. S18). Nitrogen sorption analysis of the material after 5 cycles showed no changes in shape of the isotherm and pore size distribution (Figs. S19 and S20) pointing to stable mesoporous structure.

4. Conclusion

In summary, we have systematically evaluated four parameters in the synthesis of mesoporous Nb_2O_5 using EISA with the soft-templating method: synthesis duration, airflow rate, RH and water content in the reaction mixture. The highest specific surface area and photocatalytic activity were achieved with long synthesis duration (3 days), low airflow rate and 33 % RH. In further experiments, higher water content in the reaction mixture increased the specific surface area, improved photocatalytic performance and changed pore order from hexagonal to unordered based on the TEM analysis. We identified the optimal synthesis parameters to produce amorphous Nb_2O_5 with a high specific surface area, a narrow hysteresis loop in the N_2 sorption isotherm and narrow pore size distribution centred at approx. 6 nm. The photocatalytic performance increased linearly with the specific surface area for three out of four material groups. Notably, the materials with the same specific surface area with a higher degree of order of the mesoporous structure exhibit approx. two times higher activity than the materials with a lower degree of order. The best performing material also exhibited stable activity (>90 % of initial value) over 5 cycles and no changes in the mesoporous structure. This study underscores the importance of optimising often unreported synthesis parameter such as airflow rate in the case of mesoporous Nb_2O_5. Furthermore, it underlines that in addition to the specific surface area, a well-ordered mesoporous structure plays a crucial role in maximising photocatalytic performance.

CRediT authorship contribution statement

Peter Nadrah: Writing – original draft, Visualization, Validation, Supervision, Methodology, Funding acquisition, Data curation, Conceptualization. **Mateja Knap:** Writing – original draft, Investigation, Data curation. **Erika Švara Fabjan:** Writing – review & editing, Methodology, Investigation. **Andraž Šuligoj:** Writing – review & editing, Investigation, Data curation. **Urška Lavrenčič Štangar:** Writing – review & editing, Resources, Project administration, Funding acquisition. **Goran Dražić:** Writing – review & editing, Investigation. **Nataša Novak Tušar:** Writing – review & editing, Resources, Project administration, Funding acquisition. **Andrijana Sever Škapin:** Writing – review & editing, Resources, Project administration, Methodology, Funding acquisition.

Declaration of competing interest

The authors declare that they have no known competing financial interests or personal relationships that could have appeared to influence the work reported in this paper.

Acknowledgements

We thank assoc. prof. dr. Boštjan Genorio for XPS measurements. The authors acknowledge the financial support by the Slovenian Research and Innovation Agency (Grants no. J2-4441, P2-0273, P1-0418, P1-0134 and P2-0421).

Appendix A. Supplementary data

Supplementary data to this article can be found online at https://doi.org/10.1016/j.micromeso.2025.113994.

Data availability

Data for this article are available at https://doi.org/10.5281/zenodo.15298881.

References

[1] M. B. Beg, L. Ali and M. Altarawneh: Investigating niobium oxide-based materials: synthesis, characterization, and applications in heterogeneous catalysis. Catal. Rev., 0, 1–90. https://doi.org/10.1080/01614940.2025.2564083.
[2] Y. Zhao, X. Zhou, L. Ye, S. Chi Edman Tsang, Nanostructured Nb2O5 catalysts, Nano Rev. 3 (2012) 17631, https://doi.org/10.3402/nano.v3i0.17631.
[3] C. Avcıoğlu, S. Avcıoğlu, M.F. Bekheet, A. Gurlo, Solar hydrogen generation using niobium-based photocatalysts: design strategies, progress, and challenges, Mater. Today Energy 24 (2022) 100936, https://doi.org/10.1016/j.mtener.2021.100936.
[4] R.M. Pittman, A.T. Bell, Raman studies of the structure of niobium oxide/titanium oxide (Nb2O5.TiO2), J. Phys. Chem. 97 (1993) 12178–12185, https://doi.org/10.1021/j100149a013.
[5] E. Onur, J. Lee, R. Aymerich-Armengol, J. Lim, Y. Dai, H. Tüysüz, C. Scheu, C. Weidenthaler, Exploring the effects of the photochromic response and crystallization on the local structure of noncrystalline niobium oxide, ACS Appl. Mater. Interfaces 16 (2024) 25136–25147, https://doi.org/10.1021/acsami.4c04038.
[6] W. Ji, H. Xie, B. Deng, Y. Yu, Q. Geng, Y. Cao, Y. Li, Cu metal-modified Nb2O5 microspheres boost photoreduction of CO2 to CH4 via enhanced adsorption of C1 intermediates, Ind. Eng. Chem. Res. 64 (2025) 8248–8256, https://doi.org/10.1021/acs.iecr.5c00316.

[7] A.U. Rehman, K.D. Han, M.U. Ali, Y. He, A.A. Sergeev, Z. Yuan, C. Dong, X. Gao, C. A. Not, A.M.C. Ng, K.S. Wong, Z.X. Guo, I. Lončarić, J. Popović, A.B. Djurišić, Niobium oxide for microplastics Degradation—The effect of crystal structure and morphology, Small Struct. (2025) 2500124, https://doi.org/10.1002/sstr.202500124 **n/a**.

[8] J. Wang, C. Zhou, J. Wu, T. Zhang, Facile fabrication of TT-T Nb2O5 heterophase junctions via in situ phase transformation towards enhanced photocatalytic H2-Production activity, J. Mater. Chem. A 12 (2024) 4123–4128, https://doi.org/10.1039/D3TA06599E.

[9] X. Chen, T. Yu, X. Fan, H. Zhang, Z. Li, J. Ye, Z. Zou, Enhanced activity of mesoporous Nb2O5 for photocatalytic hydrogen production, Appl. Surf. Sci. 253 (2007) 8500–8506, https://doi.org/10.1016/j.apsusc.2007.04.035.

[10] D. Rathnayake, I. Perera, A. Shirazi-Amin, P. Kerns, S. Dissanayake, S.L. Suib, Mesoporous crystalline niobium oxide with a high surface area: a solid acid catalyst for alkyne hydration, ACS Appl. Mater. Interfaces 12 (2020) 47389–47396, https://doi.org/10.1021/acsami.0c10757.

[11] I. Nowak, M. Jaroniec, "Hard" vs. "Soft" templating synthesis of mesoporous Nb2O5 catalysts for oxidation reactions, Top. Catal. 49 (2008) 193–203, https://doi.org/10.1007/s11244-008-9084-1.

[12] C.L. Ücker, V. Goetzke, F.C. Riemke, M.L. Vitale, L.R.Q. de Andrade, M.D. Ücker, E. C. Moreira, M.L. Moreira, C.W. Raubach, S.S. Cava, Multi-photonic behavior of Nb2O5 and its correlation with synthetic methods, J. Mater. Sci. 56 (2021) 7889–7905, https://doi.org/10.1007/s10853-021-05770-z.

[13] J.B.G. Filho, L.D. Almeida, H.F.V. Victória, G.H.M. Gomes, K. Krambrock, P. A. Robles-Azocar, M.C. Pereira, L.C.A. Oliveira, Niobium oxides: the key role of hydroxylated surface on photocatalytic driven C–C reductive coupling of acetophenone, J. Catal. 436 (2024) 115580, https://doi.org/10.1016/j.jcat.2024.115580.

[14] M. Souza, M. Bernardo, H. Alves, C. Silva, A. O. Patrocínio and O. Lopes: Effect of the synthesis parameters on the physicochemical properties and photocatalytic performance of Nb2O5 to water treatment and H2 production. J. Braz. Chem. Soc., DOI:10.21577/0103-5053.20230169. https://doi.org/10.21577/0103-5053.20230169.

[15] A. Ramanathan, H. Zhu, R. Maheswari, B. Subramaniam, Remarkable epoxidation activity of neat and carbonized niobium silicates prepared by evaporation-induced self-assembly, Microporous Mesoporous Mater. 261 (2018) 158–163, https://doi.org/10.1016/j.micromeso.2017.10.049.

[16] X. Bi, G. Du, A. Kalam, D. Sun, W. Zhao, Y. Yu, Q. Su, B. Xu, A.G. Al-Sehemi, Constructing anatase TiO2/Amorphous Nb2O5 heterostructures to enhance photocatalytic degradation of acetaminophen and nitrogen oxide, J. Colloid Interface Sci. 601 (2021) 346–354, https://doi.org/10.1016/j.jcis.2021.05.120.

[17] X. Deng, J. Zhang, K. Qi, G. Liang, F. Xu, J. Yu, Ultrafast electron transfer at the In2O3/Nb2O5 S-Scheme interface for CO2 photoreduction, Nat. Commun. 15 (2024) 4807, https://doi.org/10.1038/s41467-024-49004-7.

[18] L.F.W. Brum, M.D.C.R. da Silva, C. dos Santos, G. Pavoski, D.C.R. Espinosa, W.L. da Silva, Green synthesis of niobium (V) oxide nanoparticles using pecan nutshell (*Carya illinoinensis*) and evaluation of its antioxidant activity, Catal. Today 445 (2025) 115106, https://doi.org/10.1016/j.cattod.2024.115106.

[19] T. Larison, E.R. Williams, M. Wright, M. Zhang, J. Tengco, M.G. Boebinger, C. Tang, M. Stefik, One-pot self-assembly of sequence-controlled mesoporous heterostructures via structure-directing agents, ACS Nano 18 (2024) 20133–20141, https://doi.org/10.1021/acsnano.4c01855.

[20] L. Mahoney, R.T. Koodali, Versatility of evaporation-induced self-assembly (EISA) method for preparation of mesoporous TiO2 for energy and environmental applications, Materials 7 (2014) 2697–2746, https://doi.org/10.3390/ma7042697.

[21] H. Yu, M. Liu, Q. Lu, Y. Yu, D. Zhao, X. Li, Mesoporous metal oxides, J. Phys. Chem. C 128 (2024) 19945–19961, https://doi.org/10.1021/acs.jpcc.4c05815.

[22] D. Grosso, F. Cagnol, A. Soler-Illia, E.L. Crepaldi, H. Amenitsch, A. Brunet-Bruneau, A. Bourgeois, C. Sanchez, Fundamentals of mesostructuring through evaporation-induced self-assembly, Adv. Funct. Mater. 14 (2004) 309–322, https://doi.org/10.1002/adfm.200305036.

[23] D.M. Antonelli, A. Nakahira, J.Y. Ying, Ligand-assisted liquid crystal templating in mesoporous niobium oxide molecular sieves, Inorg. Chem. 35 (1996) 3126–3136, https://doi.org/10.1021/ic951533p.

[24] P. Yang, D. Zhao, D.I. Margolese, B.F. Chmelka, G.D. Stucky, Generalized syntheses of large-pore mesoporous metal oxides with semicrystalline frameworks, Nature 396 (1998) 152–155, https://doi.org/10.1038/24132.

[25] P. Yang, D. Zhao, D.I. Margolese, B.F. Chmelka, G.D. Stucky, Block copolymer templating syntheses of mesoporous metal oxides with large ordering lengths and semicrystalline framework, Chem. Mater. 11 (1999) 2813–2826, https://doi.org/10.1021/cm990185c.

[26] B. Lee, D. Lu, J.N. Kondo, K. Domen, Three-dimensionally ordered mesoporous niobium oxide, J. Am. Chem. Soc. 124 (2002) 11256–11257, https://doi.org/10.1021/ja026838z.

[27] X. Xu, B.z. Tian, J.l. Kong, S. Zhang, B.h. Liu, D.y. Zhao, Ordered mesoporous niobium oxide film: a novel matrix for assembling functional proteins for bioelectrochemical applications, Adv. Mater. 15 (2003) 1932–1936, https://doi.org/10.1002/adma.200305424.

[28] X. Xu, B. Tian, S. Zhang, J. Kong, D. Zhao, B. Liu, Electrochemistry and biosensing reactivity of heme proteins adsorbed on the structure-tailored mesoporous Nb2O5 matrix, Anal. Chim. Acta 519 (2004) 31–38, https://doi.org/10.1016/j.aca.2004.05.061.

[29] L. Yuan, V.V. Guliants, Mesoporous niobium oxides with tailored pore structures, J. Mater. Sci. 43 (2008) 6278–6284, https://doi.org/10.1007/s10853-008-2904-7.

[30] L. Ye, S. Xie, B. Yue, L. Qian, S. Feng, S.C. Tsang, Y. Li, H. He, Crystalline three-dimensional cubic mesoporous niobium oxide, CrystEngComm 12 (2010) 344–347, https://doi.org/10.1039/B913268F.

[31] W.R.K. Thalgaspitiya, T.K. Kapuge, J. He, D. Rathnayake, P. Kerns, S.L. Suib, Mesoporous molybdenum–tungsten mixed metal oxide: a solid acid catalyst for green, highly efficient Sp3–Sp2 C–C coupling reactions, ACS Appl. Mater. Interfaces 12 (2020) 5990–5998, https://doi.org/10.1021/acsami.9b21633.

[32] N. Rozman, A. Sever Škapin, D.M. Tobaldi, G. Dražić, P. Nadrah, Tailoring the crystalline and amorphous phase ratios of TiO2 through the use of organic additives during hydrothermal synthesis, Ceram. Int. 50 (2024) 37033–37040, https://doi.org/10.1016/j.ceramint.2024.07.092.

[33] N. Suzuki, T. Athar, Y.-T. Huang, K. Shimasaki, N. Miyamoto, Y. Yamauchi, Synthesis of mesoporous Nb_2O_5 with crystalline walls and investigation of their photocatalytic activity, J. Ceram. Soc. Jpn. 119 (2011) 405–411, https://doi.org/10.2109/jcersj2.119.405.

[34] K.S.W. Sing, R.T. Williams, Physisorption hysteresis loops and the characterization of nanoporous materials, Adsorpt. Sci. Technol. 22 (2004) 773–782, https://doi.org/10.1260/0263617053499032.

[35] F. Sotomayor, K. Cychosz and M. Thommes: Characterization of Micro/mesoporous Materials by Physisorption: Concepts and Case Studies. .

[36] M. Thommes, K. Kaneko, A.V. Neimark, J.P. Olivier, F. Rodriguez-Reinoso, J. Rouquerol, K.S.W. Sing, Physisorption of gases, with special reference to the evaluation of surface area and pore size distribution (IUPAC technical report), Pure Appl. Chem. 87 (2015) 1051–1069, https://doi.org/10.1515/pac-2014-1117.

[37] K.M.A. Santos, E.M. Albuquerque, L.E.P. Borges, M.A. Fraga, Discussing lewis and brønsted acidity on continuous pyruvaldehyde cannizzaro reaction to lactic acid over solid catalysts, Mol. Catal. 458 (2018) 198–205, https://doi.org/10.1016/j.mcat.2017.12.010.

[38] G.T.S.T. da Silva, A.E. Nogueira, J.A. Oliveira, J.A. Torres, O.F. Lopes, C. Ribeiro, Acidic surface niobium pentoxide is catalytic active for CO2 photoreduction, Appl. Catal. B Environ. 242 (2019) 349–357, https://doi.org/10.1016/j.apcatb.2018.10.017.

[39] H.T. Kreissl, M.M.J. Li, Y.-K. Peng, K. Nakagawa, T.J.N. Hooper, J.V. Hanna, A. Shepherd, T.-S. Wu, Y.-L. Soo, S.C.E. Tsang, Structural studies of bulk to nanosize niobium oxides with correlation to their acidity, J. Am. Chem. Soc. 139 (2017) 12670–12680, https://doi.org/10.1021/jacs.7b06856.

[40] N. Usha, R. Sivakumar, C. Sanjeeviraja, M. Arivanandhan, Niobium pentoxide (Nb2O5) thin films: rf power and substrate temperature induced changes in physical properties, Optik - International Journal for Light and Electron Optics 126 (2015) 1945–1950, https://doi.org/10.1016/j.ijleo.2015.05.036.

[41] Y. Wang, S. Aghamohammadi, D. Li, K. Li, R. Farrauto, Structure dependence of Nb2O5-X supported manganese oxide for catalytic oxidation of propane: enhanced oxidation activity for MnOx on a low surface area Nb2O5-X, Appl. Catal. B Environ. 244 (2019) 438–447, https://doi.org/10.1016/j.apcatb.2018.11.066.

[42] C.L. Ücker, F. Riemke, V. Goetzke, M.L. Moreira, C.W. Raubach, E. Longo, S. Cava, Facile preparation of Nb2O5/TiO2 heterostructures for photocatalytic application, Chem. Phys. Impact 4 (2022) 100079, https://doi.org/10.1016/j.chphi.2022.100079.

[43] F.A. Qaraah, S.A. Mahyoub, A. Hezam, A. Qaraah, F. Xin, G. Xiu, Synergistic effect of hierarchical structure and S-Scheme heterojunction over O-Doped g-C3N4/N-Doped Nb2O5 for highly efficient photocatalytic CO2 reduction, Appl. Catal. B Environ. 315 (2022) 121585, https://doi.org/10.1016/j.apcatb.2022.121585.

[44] M. Ristić, S. Popović, S. Musić, Sol–gel synthesis and characterization of Nb2O5 powders, Mater. Lett. 58 (2004) 2658–2663, https://doi.org/10.1016/j.matlet.2004.03.041.

[45] Y. Zhang, T. Song, X. Zhou, Y. Yang, Oxygen-vacancy-boosted visible light driven photocatalytic oxidative dehydrogenation of saturated N-Heterocycles over Nb2O5 nanorods, Appl. Catal. B Environ. 316 (2022) 121622, https://doi.org/10.1016/j.apcatb.2022.121622.

[46] E.I. García-López, F.R. Pomilla, B. Megna, M.L. Testa, L.F. Liotta, G. Marcì, Catalytic dehydration of fructose to 5-Hydroxymethylfurfural in aqueous medium over Nb2O5-Based catalysts, Nanomaterials 11 (2021) 1821, https://doi.org/10.3390/nano11071821.

[47] C. Tiozzo, C. Bisio, F. Carniato, A. Gallo, S.L. Scott, R. Psaro, M. Guidotti, Niobium–silica catalysts for the selective epoxidation of cyclic alkenes: the generation of the active site by grafting niobocene dichloride, Phys. Chem. Chem. Phys. 15 (2013) 13354–13362, https://doi.org/10.1039/C3CP51570B.

[48] F.D. Hardcastle, I.E. Wachs, Determination of niobium-oxygen bond distances and bond orders by Raman spectroscopy, Solid State Ionics 45 (1991) 201–213, https://doi.org/10.1016/0167-2738(91)90153-3.

[49] J.M. Jehng, I.E. Wachs, Structural chemistry and raman spectra of niobium oxides, Chem. Mater. 3 (1991) 100–107, https://doi.org/10.1021/cm00013a025.

[50] T. Shishido, T. Miyatake, K. Teramura, Y. Hitomi, H. Yamashita, T. Tanaka, Mechanism of photooxidation of alcohol over Nb2O5, J. Phys. Chem. C 113 (2009) 18713–18718, https://doi.org/10.1021/jp901603p.

[51] T. Onfroy, G. Clet, M. Houalla, Correlations between acidity, surface structure, and catalytic activity of niobium oxide supported on zirconia, J. Phys. Chem. B 109 (2005) 14588–14594, https://doi.org/10.1021/jp0517347.